Tailoring the Open Circuit Voltage Deficit of Wide Bandgap Perovskite Solar Cells Using Alkyl Chain Substituted Fullerene Derivatives

Dhruba B. Khadka[a,b*], Yasuhiro Shirai[b*], Masatoshi Yanagida[b], Takeshi Noda[c] and Kenjiro Miyano[b]

[a] *International Center for Young Scientists (ICYS), National Institute for Materials Science (NIMS), 1-1 Namiki, Tsukuba, Ibaraki 305-0044, Japan.*

[b]*Global Research Center for Environment and Energy based on Nanomaterials Science (GREEN), National Institute for Materials Science (NIMS), 1-1 Namiki, Tsukuba, Ibaraki 305-0044, Japan.*

[c]*Photovoltaic Materials Group, National Institute for Materials Science (NIMS), 1-2-1 Sengen, Tsukuba, Ibaraki 305-0047, Japan.*

ABSTRACT

Wide bandgap perovskite devices are promising as the top cell of silicon-perovskite tandem devices to boost the efficiency beyond the Shockley-Queisser limit. Here, we tailor the performance parameters of wide bandgap (WB) mixed halide perovskite solar cell with long alkyl chain substituted fullerene derivatives as an electron transport layer (ETL). The device with C60-fused N-methylpyrrolidine-meta-dodecyl phenyl ($C_{60}MC_{12}$) demonstrates an enhanced power conversion efficiency of 16.74 % with the record open circuit voltage (V_{OC}) of 1.24 V; an increase by 70 mV with concomitant V_{OC} deficit reduction to 0.47 V. This is achieved by mitigating the recombination loss through the use of highly crystalline $C_{60}MC_{12}$ film compared to amorphous PCBM layer. The device analysis reveals the soothing of the defect activities with shallower defect states and passivation of the interface recombination centers for the device with $C_{60}MC_{12}$. We ascribe this property to the crystallinity of fullerene derivatives as ETL, which is also important for optimizing device parameters, besides the band alignment matching of WB perovskite devices.

Keywords: Wide bandgap, fullerene derivatives, crystallinity, V_{OC} deficit, defect

1. INTRODUCTION

Multi-junction tandem solar cells are promising technological pathway to realize power conversion efficiency (PCE) higher than that achievable with single junction cells.[1] One possible scenario toward tandem cells is to exploit the existing industry of inorganic PVs, namely to use a Si solar cell as a bottom cell.[2,3] Crystalline Si (c-Si) with a bandgap of about 1.12 eV requires an absorbing layer with a bandgap of about 1.7-1.8 eV to generate a matching photocurrent density (J_{SC}) of ~20 $mAcm^{-2}$ which leads to a potential improvement of PCE beyond the theoretical limit.[4,5] A photovoltaic material with wide bandgap (WB) tunability is suitable for the tandem top cell only if it has high performance and low temperature cost effective processability so that Si-tandem structure can be fabricated without significantly raising the cost.[6–8] Indeed, lead halide perovskite single-junction solar cells have already achieved device efficiency exceeding ~22% with low processing cost.[9] This material possesses excellent optoelectronic properties and bandgap (E_g) tunability (~1.5 to 2.3 eV)[6,10–13] which allows a wide selection range of ideal photovoltaic materials for the tandem device application. This merit of organometal trihalide perovskite material makes promising candidates for the top cell. Nevertheless, the device efficiency of silicon/perovskite monolithic tandem cell[7,8] is still much low compare to the silicon solar cell (~27%) due to the limited performance of the WB perovskite top cells.[6,14–16]

A number of efforts have been made to enhance the performance of the WB ($1.7 \leq E_g \leq 1.8$ eV) perovskite solar cells (PSCs) by tuning the bandgap of $MAPbI_3$ perovskite material.[6,11,12,17–22] Though multiple reports demonstrated comparable fill factor (*FF*) and quantum spectrum for narrower and WB PSCs, the suppression of the open circuit voltage (V_{OC}) is the main issue for WB perovskite devices.[6,15] Note that the V_{OC} deficit ($\Delta V_{OC} = E_g/q - V_{OC}$) of narrower bandgap ($E_g \leq 1.6$ eV) perovskite device is ≤ 0.4 V tailored with morphology and composition,[18,23–25] whereas it is in the range of ≥ 0.50 V for WB PSCs.[6,14] This impedes the

enhancement of the tandem device efficiency. Note that multiple reports suggested the phase separation of WB mixed halide perovskites ($MAPb(I_{1-x}Br_x)_3$) under illumination.[12,26–30] The photo-induced phase segregation was cogitated to be detrimental for V_{OC} deficit in WB perovskite device due to the traps induced with compositional non-uniformity and formation of sub bandgap phase. Recently, Snaith and co-workers reported WB perovskite ($E_g \geq 1.7$ eV) solar cells of high efficiency ~17 % using the $(FA,Cs)Pb(I_{1-x}Br_x)_3$ perovskite layer having thermal and photo-stability.[6] However, there is still large V_{OC} deficit ~0.54 eV which indicates additional limiting factors. Considering that point, Huang and co-workers demonstrated WB perovskite ($E_g \geq 1.7$ eV) device of a record PCE ~18.5% using stabilized perovskite material having mixed composition of $(FA,MA,Cs)Pb(I_{1-x}Br_x)_3$ by tuning the carrier transport layers (CTLs); indene-C60 bisadduct (ICBA) having reduced energy disorder.[15] The V_{OC} deficit was lowered to ~0.5 eV. Concerning the V_{OC} limiting issue, the studies on the impact of CTL on device characteristics of WB perovskite device can provide guidelines for further improvements.

Herein, we report the improvement in WB (E_g ~1.71 eV) perovskite ($MAPb(I_{1-x}Br_x)_3$; x~0.27) device by tuning the electron transport layers (ETLs) with highly crystalline fullerene derivatives. The device with long-chain alkyl substituted fullerene derivative, C60-fused N-methylpyrrolidine-meta-dodecyl phenyl [($C_{60}MC_{12}$), hereafter CMC] as an ETL demonstrated a record V_{OC}=1.24 V (PCE~ 16.74%) with reduced V_{OC} deficit to ~0.47eV. The better crystal quality and superior electrical properties of CMC over PCBM are beneficial for mitigation of energy disorder in CTLs and soothing the recombination activities. This minimizes the V_{OC} loss and enhances the device performance. We investigated the enhancement in performance of WB perovskite devices by optoelectronic characterizations.

2. RESULTS AND DISCUSSION

To confirm the proper wide bandgap tuning condition, mixed halide $MAPb(I_{1-x}Br_x)_3$ perovskite (mixed HaP) thin films were prepared adopting Cl-mediated interdiffusion approach[31] by varying weight percentage of MAI and MABr in the precursor solutions. The details of fabrication process have been described in the experimental section (Supporting Information). Figure 1a depicts a magnified view of dominant characteristic XRD peaks of mixed HaP films (Fig. S1a). A gradual shift of all XRD peaks to larger diffraction angles (depicted as an inset in Fig. 1a and Fig. S1b3) and a decreasing trend of lattice constant (Fig. S1b1) with increasing MABr content (as depicted in Fig. 1a inset), indicate incorporation of Br into the crystal lattice to form mixed HaP films. This trend agrees with other reports.[10,13,33] A slight increasing trend in the full width at half maximum (FWHM) for MABr content (100%) (Fig. S1b2) reflects the decrease in crystal quality. Figure 1b shows the absorption spectra of respective films. The estimated bandgaps (E_g) (depicted in inset Fig. 1c) increase monotonically with increasing MABr content in the precursor solution. We fitted the estimated E_g with band bowing equation reported by Seok and co-workers,[10] $E_g(x) = E_g\ (x=0) + 0.39x + 0.33x^2$, where x is bromine composition. The Br content (x) incorporated into the mixed HaP film are extracted from the plot (Fig. 1c). It varies x~0- 0.44 corresponding to MABr content 0-100%. It is found that the MABr content percentage (50%) is equivalent to Br composition; x~0.27 in $MAPb(I_{1-x}Br_x)_3$ perovskite film which gives a proper band gap (~1.71 eV) for top cell in tandem structure.[6,20]

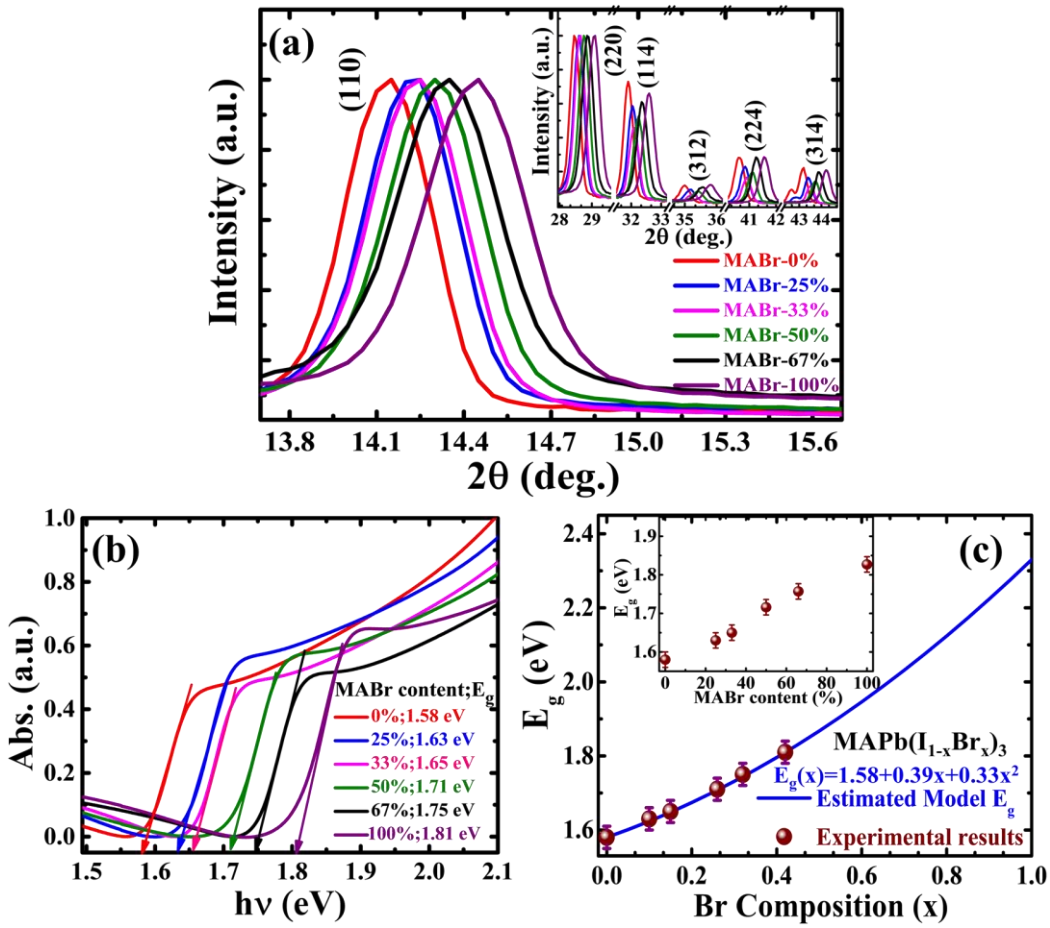

Figure 1. XRD patterns (magnified view) (a) and absorption spectra (b) of mixed HaP films. The plot of bandgap energies (E_g) estimated from plot (b) and fitted with band bowing model[10] (c). Inset in Fig. c displays a variation of E_g of mixed HaP films fabricated by varying MABr content in the precursor solution.

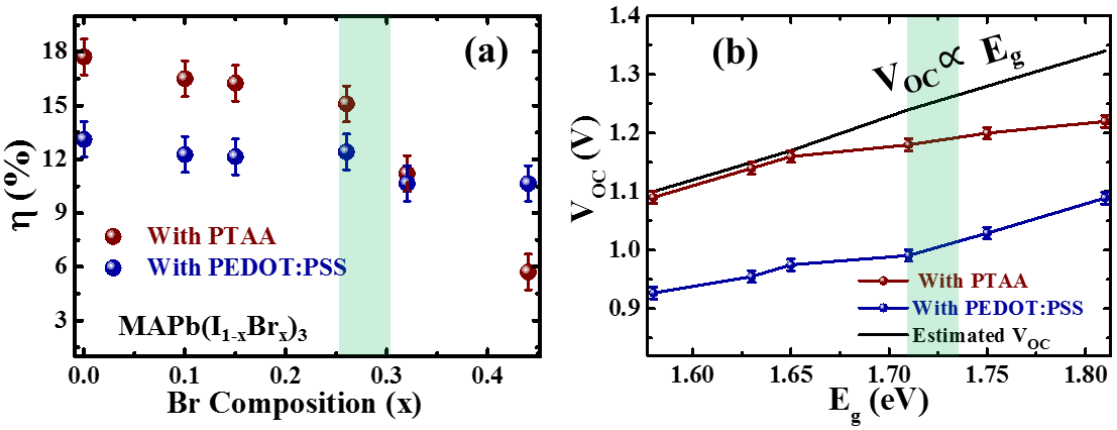

Figure 2. The PCE of devices employing hole transport layers (HTLs); PEDOT:PSS and PTAA with Mixed HaP films by varying MABr content in the precursor solution (a). The

shaded region represents the better performance range for WB $MAPb(I_{1-x}Br_x)_3$ perovskite device suitable for Si-perovskite tandem device. The trend of V_{OC} with increase in E_g of the perovskite film for both devices and estimated V_{OC} with respect to increase in E_g (solid line) (b). The estimated V_{OC} is calculated with the reference of the V_{OC} for E_g *(x=0)* with proportional increment in E_g of mixed HaP films in PSCs.

After tuning the band gap of perovskite, we fabricated a complete device using respective perovskite layer and CTLs adopting our usual device structure as described in our earlier reports.[31,32] We employed PEDOT:PSS and PTAA as HTL for a set of Br varied perovskite layers coupled with PCBM as ETL for both cases. Figure 2 shows the PCE of respective devices. The trend of PCE (Fig. 2a) exhibits a good agreement with the report by Seok and co-workers.[10] We observed a noticeable increase in V_{OC} (Fig. 2b) for all Br varied perovskite devices with PTAA compared to the PEDOT:PSS devices which is in a good agreement with the reports.[14,20,34] The lower performance of device with PEDOT:PSS is not surprising. The suppression of V_{OC} for perovskite device with PEDOT:PSS (Fig. 2b) is attributed to the deleterious HTL/perovskite interface[35,36] or perovskite film quality grown on HTL.[14,32] Our previous study suggested that the V_{OC} reduction for the device with PEDOT:PSS compared to PTAA as an HTL is dominantly influenced by the recombination at perovskite/PEDOT:PSS interface and higher defect profile in perovskite layer grown on it.[32] The WB (E_g~1.71 eV, x~0.27) $MAPb(I_{1-x}Br_x)_3$ perovskite solar cells (here after, WB PSCs) with PTAA demonstrated an efficiency of 15.11 % (V_{OC} ~1.17 V, J_{SC}~16.46 $mAcm^{-2}$) with large V_{OC} deficit ~0.54 V. The WB perovskite device with PTAA can be further improved by reducing the V_{OC} loss from the estimated trend (Fig. 2b) and increasing the photocurrent. Despite the fact that the phase segregation of WB mixed HaP under prolonged illumination is deleterious,[27,28] the V_{OC} loss was still found to be dominant even for stabilized WB perovskite phase indicating that the phase stability is not impugning factor.[6,15] So, it is crucial to improve the V_{OC} and explore the limitation factors for WB PSCs.

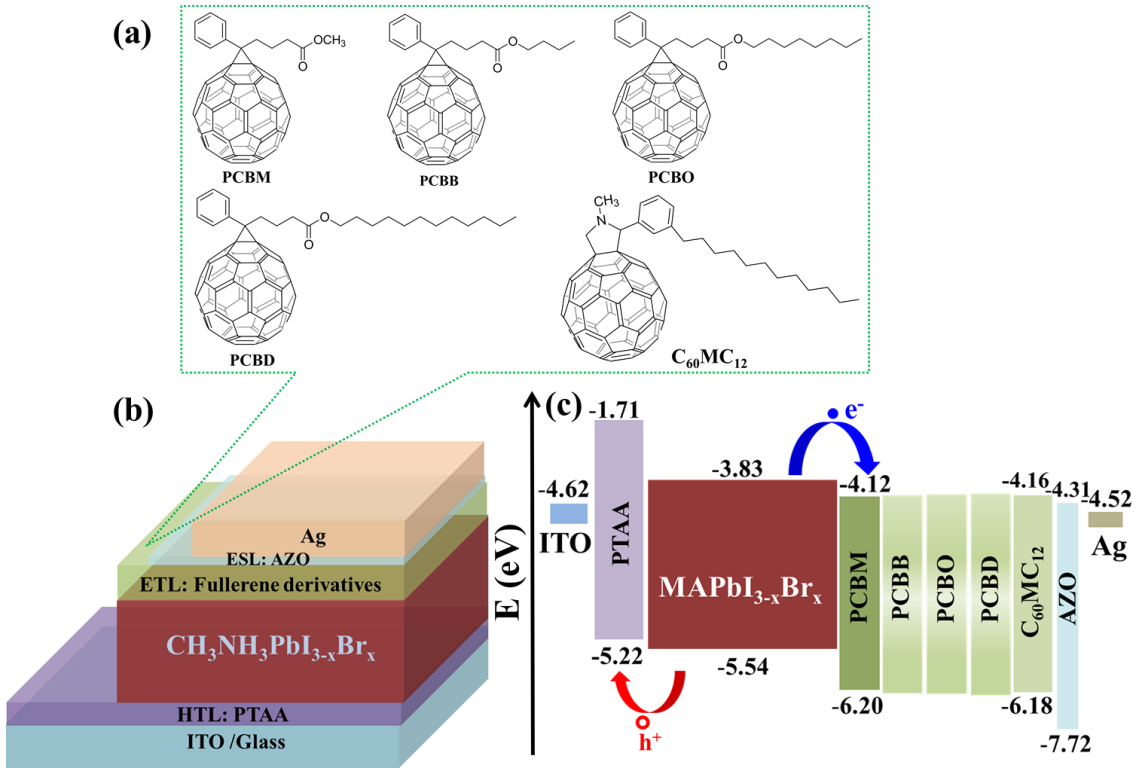

Figure 3. (a) Molecular structure of long-chain alkyl substituted fullerene derivative, (b) schematic of the planar PSC, and (c) band alignments diagram (estimated by photoelectron spectroscopy) of the inverted PSC.

The V_{OC} of WB perovskite device is affected by a number of factors such as the band alignment, crystallinity, disorder energy of CTL,[15,24] besides the morphology and crystal quality of perovskite layer.[14,37,38] Some studies revealed that the defects in the perovskite layer also influence the V_{OC} deficit.[39,40] A report by Correa-Baena et al.[41] suggested that the dopant concentration of CTL (i.e. HTL), deposited on perovskite layer plays important role in recombination dynamics and hence limits the V_{OC} in PSCs. Following those points, we explored optimization of ETL to reduce the V_{OC} deficit of our inverted perovskite device. Indeed, only few ETLs; inorganic materials (TiO_2 and SnO_2)[42–44] and organic materials (fullerene derivatives)[45–48] have been widely used due to efficient transport of the photogenerated electrons. An added benefit with fullerene based ETLs is its passivating properties that eliminate the photocurrent hysteresis.[45,49,50] Note that the fullerene derivatives bearing various

functional group side chains have been widely employed as the ETLs in organic PV devices.[51–53] The side chains affect the properties of PCBM (energy band, optoelectronic properties, crystallinity) which can also influence the device performance.[48,52] Regarding these aspects, we studied the long chain alkyl substituted fullerene derivatives as ETLs.

Figure 3a depicts the molecular structures of long-chain alkyl substituted fullerene derivatives in the form of increasing alkyl chain in side chain of PCBM (PCBB, PCBO and PCBD) studied in this paper. The long alkyl chain in side chain of PCBM causes negligible change in energy gap with a small impact on HOMO or LUMO levels (Fig. 3c). The Nakanishi et al. reported that the alkyl chains have very small effect on molecular orbitals (MOs) of fullerene cage.[52] Obviously, the matching of band alignment is prerequisite for selection of CTLs. It can be further optimized by tuning the electronic properties and crystallinity of CTLs. The studies by Huang and co-workers showed a comparable V_{OC} irrespective of LUMO levels of fullerene derivatives in narrower band gap $MAPbI_3$ PSCs[54] whereas a larger V_{OC} was achieved in WB perovskite device with a shallower LUMO level of fullerene derivatives having lower energy disorder.[15] Although the CTL having optimal band alignment and energetic disorder of CTL is important to improve the PCE of WB PSCs, the lower energetic disorder might be rather important than perfect band matching. To evaluate those facts, we fabricated WB perovskite devices (Fig. 3b) by employing the PCBM with long alkyl chains as ETLs. Figure 4a depicts the *J-V* characteristics of respective devices (performance parameters, Table S1). Interestingly, despite of the comparable $J_{SC,}$ the devices demonstrated a lower V_{OC} with additional alkyl chains. This can be due to decrease in crystallinity with additional alkyl chains in PCBM. No crystalline peak was detected in XRD pattern (Fig. 4b) of the PCBM film, indicating amorphous nature. This agrees with the earlier reports.[24,55] Shao et al.[24] suggested that the amorphous PCBM film has a higher energetic disorder at interface which supresses the V_{OC} of device. Note that we observed no difference in XRD patterns of the PCBM film under

solvent or thermal annealing and corresponding device parameters. Moreover, the photocurrent hysteresis was predominantly observed for device with long alkyl chains (PCBD) which could also be the consequence of the increasing amorphous nature of PCBM. This will be further discussed in the succeeding paragraph.

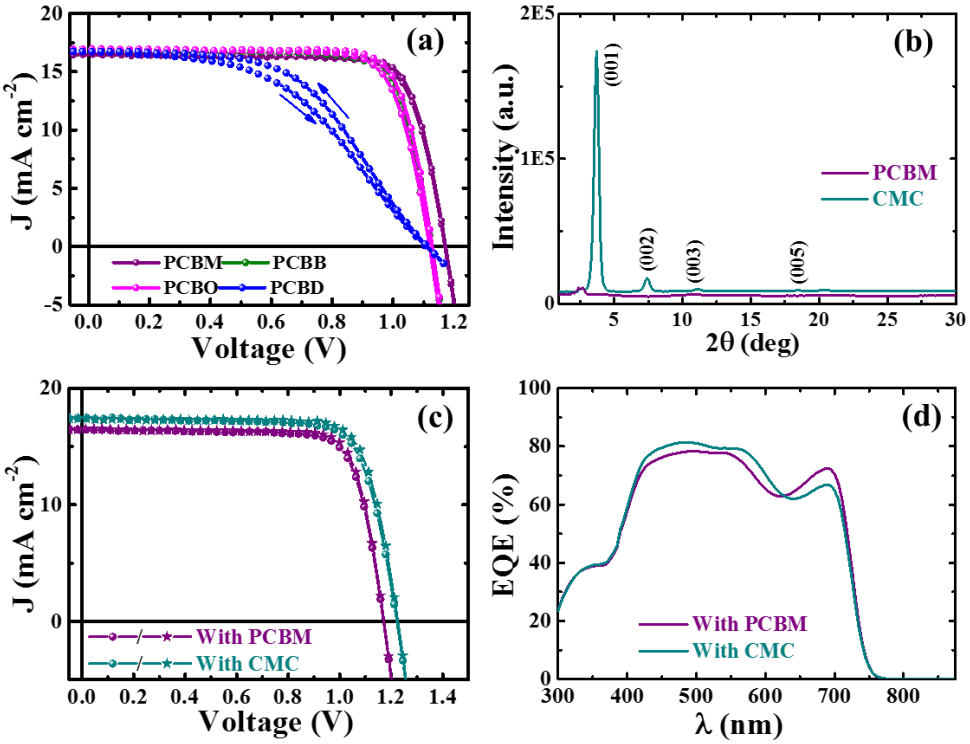

Figure 4. Current density- voltage (*J-V*) characteristics (arrows shows scan direction) of WB (E_g~1.71 eV; x~0.27; $MAPb(I_{1-x}Br_x)_3$) perovskite solar cells (WB PSCs) with long alkyl chain PCBM derivatives (a), XRD patterns of the PCBM and CMC thin films (b), *J-V* characteristics of best WB (E_g~1.71 eV) perovskite devices with PCBM or CMC as ETL (symbol stands for forward/reverse scan direction) (c) and EQE spectra of respective devices (d).

Table 1. Device parameters/ properties of WB PSCs with PCBM or CMC as ETL. J_{SC}: short circuit current density, V_{OC}: open circuit voltage, *FF*: fill factor, η: power conversion efficiency, R_S: series resistance, R_{Sh}: shunt resistance, *A*: diode ideality factor, J_0: reverse saturation current density, and * estimated from V_{OC}-*T* plot.

Device	J_{SC} ($mAcm^{-2}$)	V_{OC} (V)	*FF*	η (%)	R_S ($\Omega \cdot cm^2$)	R_{Sh} ($\Omega \cdot cm^2$)	$\Delta V_{OC} = E_g/q - V_{OC}$ (V)	$^*E_A$ (eV)
With PCBM	16.46	1.17	0.78	15.11	5.85	5.62×10^3	0.54	1.83
With CMC	17.45	1.24	0.77	16.74	5.82	4.52×10^3	0.47	1.85

In order to shed light on the role of crystallinity of fullerene derivatives for tailoring the V_{OC}, we introduced long-chain alkyl substituted fullerene derivative, CMC as an ETL. Note that CMC was used for organic electronics.[56–58] It is known for highly crystalline films with high electron mobility[55,56,58,59] which is beneficial to improve the interface and carrier transport in perovskite device. The XRD patterns (Fig. 4b) demonstrate the high crystallinity of the CMC film compared to the PCBM film. These results agree with the earlier reports.[55,56,58] The lattice spacing of the (001) plane in the CMC film is ~2.34 nm. It agrees with the reported value.[55] The absorption, transmission, photoelectron spectra (Fig. S2) are alike for both films. The surface images of the PCBM and CMC thin films and cross-sectional images of the WB PSCs with respective ETL (Fig. S3) have almost identical feature. The typical J-V characteristics (Fig. 4c, Table 1) demonstrated an improvement in PCE from 15.11 to 16.74 % for the device with CMC. This enhancement in PCE mainly stems from increase in V_{OC}~1.24 V with slight increase in J_{SC}. Importantly, the device with CMC lowered the V_{OC} deficit to 0.47 V which is lowest among the reported WB perovskite devices.[6,15] The device parameters (Fig. S4 and Table S2) show high reproducibility for large set of devices. This result indicates that the crystallinity of fullerene derivative has noticeable influence for enhancement in V_{OC} of the WB device. Cohen and co-workers[60] suggested that the disorder more likely to be present in amorphous transport layers introduces a broad distribution of traps which affects the

photovoltage and recombination in solar cells. It is speculated that the crystalline material has very weak static or dynamic disorder which minimize the tail states. This consequence could be the crucial for enhancement in V_{OC} of WB PSCs with the crystalline CMC layer. In the similar scenario, Huang and co-workers also observed a correlation between the crystallinity of the PCBM film and enhancement in V_{OC} of perovskite device.[24] The crystalline CMC thin film has higher mobility compared to amorphous PCBM film.[56,59] It is reported that mobility of carrier transport layers have impact on J_{SC}.[61] Therefore, it is speculated that a slight increase in J_{SC} (16.46 to 17.45 $mAcm^{-2}$) is the consequence of higher mobility of the CMC film. Despite achieving a record V_{OC}, the photocurrent is still lower by ~2.5 $mAcm^{-2}$ compared to matching photocurrent density (20 $mAcm^{-2}$) for tandem device structure. This could be due to thinner perovskite layer (~300 nm) in device structure compared to other reports.[6,15] The J_{SC} of our device can be enhanced by further optimization of WB perovskite layer with mixed cations and CTLs. Interestingly, though the photocurrent hysteresis appeared dominantly in devices with C_{12} alkyl in side chain of PCBM (PCBD) (Fig. 4a), the device with CMC is hysteresis free (Fig. S5). This is presumed to be related to the high crystallinity of the CMC film which may decrease the energy disorder. The PCBD film having more amorphous nature than PCBM increases energy disorder at interface.[24] It widens the band tail electronic states and activates the surface and grain boundary charge traps.[45] This induces the photocurrent hysteresis. Figure 4d displays the external quantum efficiency (EQE) spectra of respective devices, whose integration yields a similar value to J_{SC} from *J-V* curve. The CMC device revealed an enhanced EQE response in the range of ~ 400- 600 nm which is attributed to the mitigation of traps at interface and increase in mobility of the CMC film due to its high crystallinity as discussed earlier. A slight increase in EQE between 600-700 nm for the PCBM device is due to the comparatively lower reflectance (Fig. S6a).

Moreover, we also tested the stability of encapsulated devices under continuous 1 sun illumination (no UV-light filtering) and MPPT condition at 30 °C. There is no significant difference on degradation of the device parameters for the PCBM and CMC devices (Fig. S7) for short time testing. Obviously, there is degradation on the device performance after some hours. Many research groups have reported noticeable progress in device stability by mixed cations/halide perovskite[18] and engineering the CTLs[62–64] and electrodes.[65] Note that the discussion on the stability issue is beyond the scope of this work.

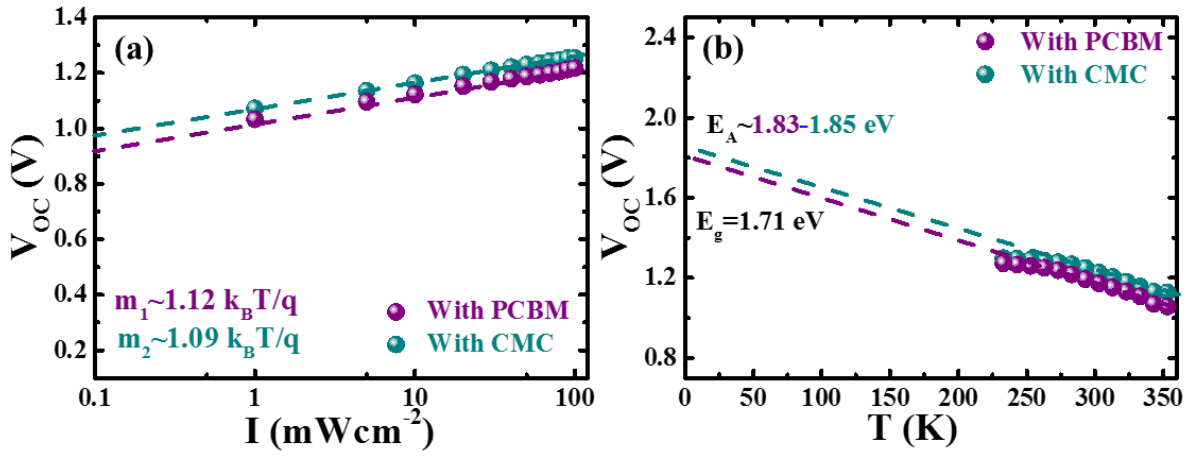

Figure 5. Plots of V_{OC}-light intensity (I) (a) and V_{OC}-T of the WB PSCs with PCBM or CMC as ETLs.

To get further insight, we investigated the operating mechanism of the WB perovskite device with PCBM and CMC as ETL. The *J*-*V* curves of devices were measured under various light intensity (*J*-*V*-*I*) (Fig. S8) to explicate the recombination of photogenerated carrier under open circuit condition. Figure 5a displays a semilogarithmic plot of V_{OC} as a function of light intensity (I) for both devices. The slopes from were estimated to be 1.12 k_BT/q and 1.09 k_BT/q for the PCBM and CMC devices, respectively. This suggests that both devices slightly suffered from trap-assisted recombination under device operation.[31,66] In addition, the energy shift ($\Delta E = E_g - E_c$; E_c is intercept of V_{OC}-I plot; for I=0) [32,66] is calculated to be ~0.59 eV

for the PCBM device which is higher than that for the CMC device (~0.52 eV). This energy shift is related to higher energetic disorder near perovskite/CTL interface.[24,66] It also supports that the PCBM device has higher energy disorder which causes the V_{OC} loss. Furthermore, the temperature dependent *J-V* curves (*J-V-T*) (Fig. S8) were studied in the temperature range of 233 to 353 K to avoid the change in perovskite phase.[67] The V_{OC}- *T* (Fig. 5b) plots explicate about the recombination mechanism that supresses V_{OC}[32,68,69] as we have demonstrated in our previous reports for narrower band gap perovskite device based on $MAPbI_3$.[32,69] The intercept of V_{OC}-*T* plot to 0 K gives the activation energy (E_A) of the recombination. The depression of E_A from E_g indicates the strength of the defect-mediated recombination at the interface due to defective layer induced in the perovskite layer.[68,69] The values of E_A were estimated to be ~1.83 and 1.85 eV for the PCBM and CMC device, respectively which are higher than E_g of perovskite film estimated from EQE spectra of respective devices (Fig. S6b). This suggests the recombination in the perovskite layer is dominant. Despite the improved interface induced by highly ordered CMC layer at ETL side, there is no noticeable difference in E_A for the PCBM and CMC devices. It has been documented that the bulk and interface quality of perovskite devices are dominantly influenced by CTL on which perovskite layer is prepared[14,32,70] rather than that deposited over perovskite absorber. It believed that our devices have dominant influence of identical interface quality induced at PTAA side for both devices induced during the device fabrication and hence the effect at interface induced by of quality of CMC film may not be so noticeable. Therefore, we presume that these devices might be differed by the traps states and densities in the perovskite film and interface effect induced by quality of ETL.

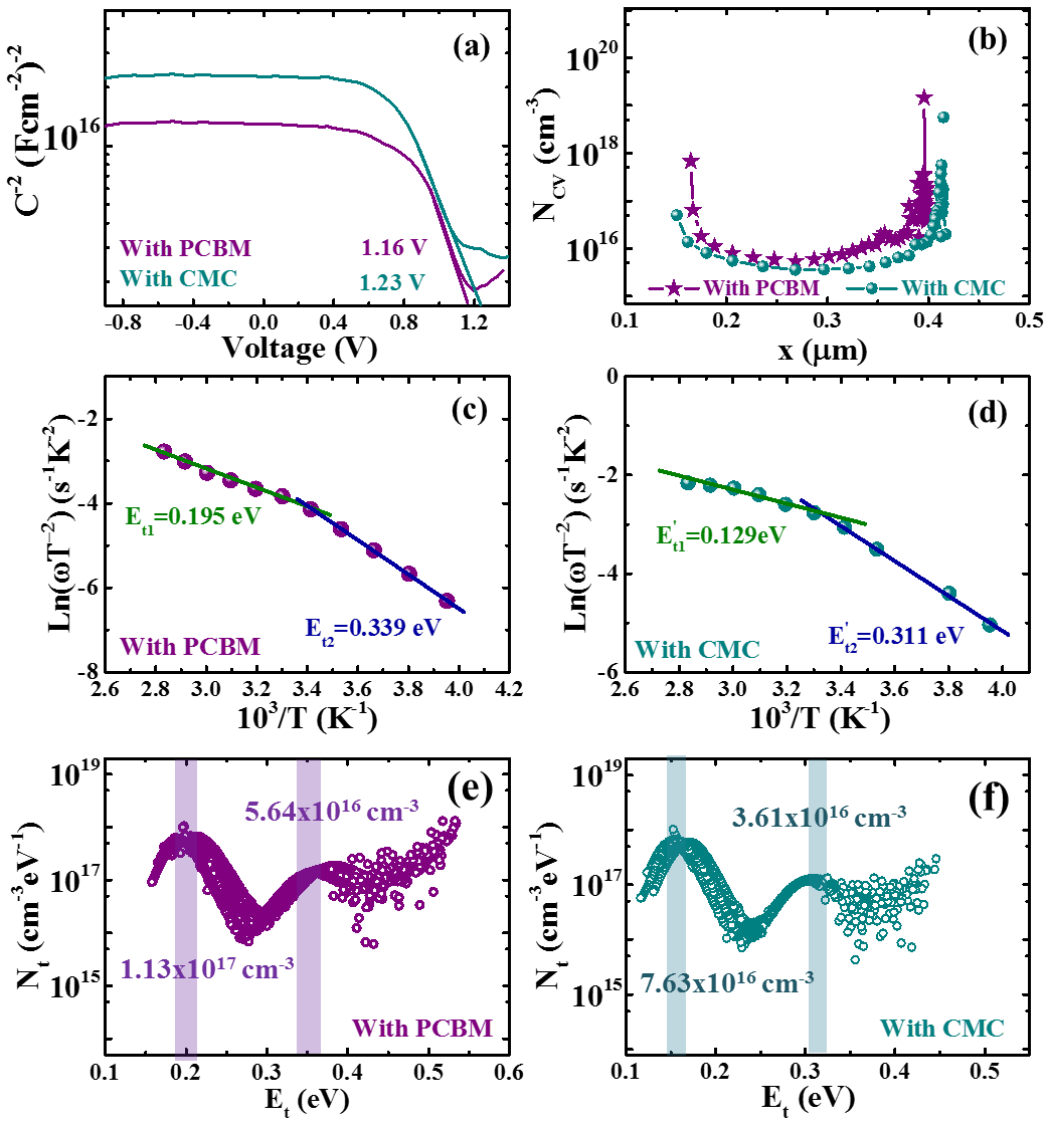

Figure 6. Capacitance spectroscopy of the WB PSCs with PCBM or CMC as ETLs. (a) Mott-Schottky (*M-S*) plot, (b) space charge carrier density and the Arrhenius plots (c, d) and defect density (N_t) profiles (e, f) for the respective devices.

In order to elucidate the characteristics origin of the two devices, we further explored the capacitance spectroscopy. This technique is commonly used to estimate the defect density, defect state and carrier density.[69,71–73] The Mott-Schottky plot (Fig. 6a) for both devices revealed a voltage independent full depletion curve indicating intrinsic junction.[68] Importantly, the diffusion potential (V_D)[31,68] for the CMC device (1.23 V) is higher than that for the PCBM device (1.16 V). This is consistent with the V_{OC} trend. In addition, the space charge carrier

profile (Fig. 6b) shows slightly higher carrier density for the PCBM device. This may be due to additional contribution from defect states induced at PCBM interface due to amorphous nature.[24,56]

We further investigated the defect induced in perovskite layer by analyzing the capacitance spectra (Fig. S9) of devices. The Arrhenius plots (Fig. 6c, d) and defect profile (Fig. 6 e, f) were estimated from using the relation,[71]

$$\omega_0 = 2\upsilon_0 T^2 e^{-E_t/k_B T} \quad (1)$$

$$N_t = -\frac{V_{bi}}{ew}\left(\frac{\omega}{k_B T}\frac{dC}{d\omega}\right) \quad (2)$$

where υ_0, E_t, C, V_{bi}, w, ω and k_B stand for the emission factor comprising all the temperature independent parameters, defect states, capacitance, built in potential, SCR width, scan frequency and Boltzmann's constant. The CMC device demonstrated comparatively shallower defect states at E_{t1}'~129 meV (υ_1'~1.12×10^7 s^{-1}) and E_{t2}'~311meV (υ_2'~1.05×10^{10} s^{-1}) whereas the defect states for the PCBM device were E_{t1}~195 meV (υ_1~3.53×10^7 s^{-1}) and E_{t2} ~339 meV (υ_2~1.08×10^{10} s^{-1}). Note that the values in parentheses are the emission factors (υ) for each defect states. Although the defect states are unlikely to specify uniquely either in bulk or close to the CTL/perovskite interface, these are presumed to be distributed near to the interface mostly. The defect densities (Fig. 6e, f) were found slightly lower (integrated defect densities; ~3.61×10^{16} and ~7.63×10^{16} cm^{-3}) for the device with CMC compared to that for the PCBM device (~5.64×10^{16} and 1.13×10^{17} cm^{-3}). Our results are found to be within the range of the report by Huang and co-workers.[15] The defect states and density profile are in the range of reported values for narrower E_g perovskite based on $MAPbI_3$.[31,32,74] It implicates the identical nature of defects induced in perovskite devices. Moreover, the defect density distribution for the PCBM device is wider compared to the CMC device. Note that both devices prepared on PTAA substrate have identical interface junction at HTL side. This implies that the suppression of defect states and defect densities for the CMC device stems from the improved interface

junction near ETL. It suggests that a high crystallinity (ordered molecules) of ETL contributes to the passivation of interface defect activities in the device. Despite having different device structure, our result agrees with the observation by Correa-Baena et al. that suggests the importance of better carrier transport materials with more selective properties for suppression of interface recombination.[41] Moreover, the numerical simulations using SCAPS[32,75] were carried out by taking into account the optoelectronic properties from device analysis (defect distribution, crystallinity of ETL and interfacial traps). Despite having some differences in figures of merit, the simulated J-V characteristics (Fig. S10, Table S3) demonstrated a close agreement with our experimental results. It supports our hypothesis that the crystalline ETL alleviates the trap centers at the interface which suppresses the recombination activities.

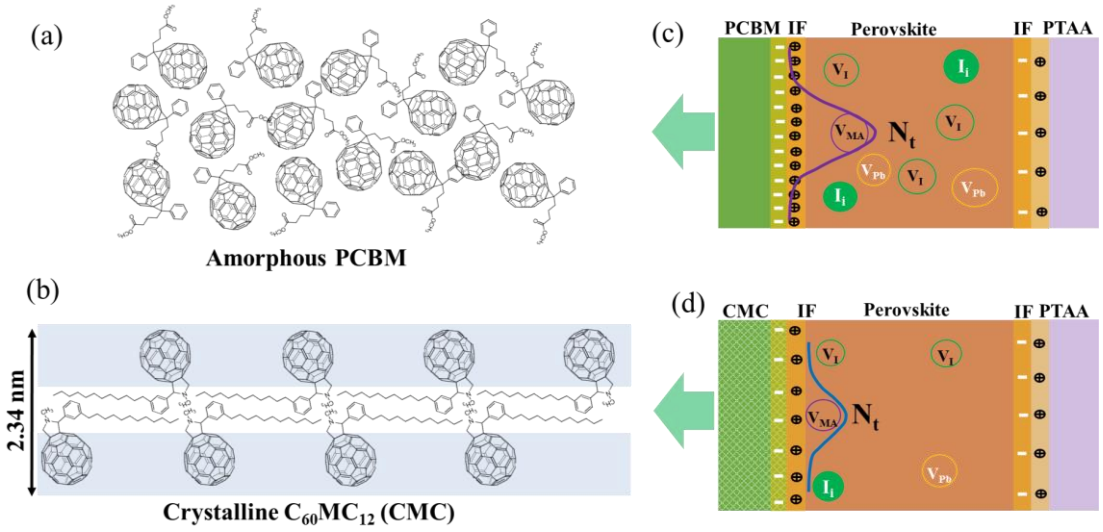

Figure 7. Schematic illustration of mechanism for enhancement in device performances with crystalline fullerene derivatives. Schematic diagrams of film structure of amorphous PCBM (a) and crystalline CMC (b) thin film. The CMC film forms 2.34 nm period bilayer structures. Schematic of detrimental charges induced at interfaces and defect species in the perovskite layer for device with amorphous (c) and crystalline (d) carrier transport layers. The filled and empty symbols represent defect species. The Gaussian distribution profile indicates the defect distribution in each device.

We propose the schematic diagrams (Fig. 7) to illustrate the phenomena behind the improvement in performance parameters for WB perovskite device with high crystallinity

CMC as an ETL. We presumed the surface molecules are randomly oriented in the amorphous PCBM film (Fig. 7a) whereas the crystalline CMC film forms well-ordered CMC molecules with periodic bilayer structure with interlaced dodecyl chains as depicted in Fig. 7b. Yase and co-workers reported that the π-π intermolecular overlap between C_{60} components facilitates the square lattice with a two-dimensional of C_{60} components in the CMC film.[55] The material having highly ordered crystalline film minimizes the static or dynamic disorder which passivates the tail states in the organic film and Fermi level pinning on other substrates.[60] The CMC thin film having bilayer crystalline structure form more favourable perovskite/ETL interface layer which is beneficial for effective carrier transport and mitigation of traps at interface. As depicted in Fig. 7c and d, both perovskite devices form the same interface quality at HTL side (PTAA/perovskite interface) whereas the ETL/perovskite interfaces differ. The device with amorphous PCBM (Fig. 7c) accumulates more detrimental charges at PCBM/perovskite interface and induces higher defect densities in the perovskite film. The defect distribution may also diffuse into the PCBM layer as well as perovskite layer as depicted in Fig. 7c. This lowers the V_{OC} of the device. On the other hand, the device with high crystallinity CMC film (Fig. 7d) forms better interface quality at CMC/perovskite interface and passivates the defect levels and defect densities in the perovskite film. Thus, the crystalline ETL film could alleviate the V_{OC} loss and improve the photocurrent by soothing the recombination activities at interface and perovskite layer. This opens the possibility of further optimization of perovskite device by tuning crystallinity of the carrier transport layer.

3. CONCLUSIONS

The wide bandgap perovskite cells are promising for silicon-perovskite tandem device to overcome the Shockley-Queisser limit owing their solution processability and bandgap tunability. We demonstrated an enhanced efficiency of 16.74 % with record V_{OC} (1.24 V)

increased by 70 mV with reduced V_{OC} deficit of 0.47 V for the WB (E_g~1.71 eV) MAPb $(I_{1-x}Br_x)_3$ perovskite devices with CMC having high crystallinity as an electron transport layer (ETL). The device characteristics; *J-V* analysis, capacitance spectroscopy revealed that the WB perovskite device with CMC alleviated the defect activities with shallower defect states (~0.129 and ~0.311 eV) and lower recombination centers ($4\text{-}7\times10^{16}$ cm^{-3}) while those for the device with PCBM were comparatively higher due to its amorphous nature. This report establishes that the WB perovskite device can be improved by matching energy band as well as crystallinity of the carrier transport layer.

4. EXPERIMENTAL DETAILS

4.1. Materials and Preparation:

All reagents and solvents were purchased from commercial suppliers as mentioned and used as received without further purification unless otherwise stated. Methyl ammonium halides (MAI, MABr, and MACl) and PbI_2 were bought from Wako chemical company. The materials such as PTAA, PCBM, PCBB, PCBO, PCBD and $C_{60}MC_{12}$ were purchased from Sigma Aldrich for carrier transport layer. The details of preparation of precursor solution and device fabrication are described in the earlier reports.[31,32] It also has been briefly mentioned supporting information.

4. 2. Material and Device Characterizations

The XRD patterns were studied using an X-ray diffractometer (Rigaku SmartLab, Japan, CuK_α, λ= 1.54050$\dot{A}$). The SEM images were obtained using a high resolution scanning electron microscope (SEM) at 5 kV accelerating voltage (Hitachi, S-4800). The absorption spectra were collected using UV-Vis-NIR spectrometer (7200, V-Jasco). HOMO levels of transport layers were collected using a photoelectron spectrometer (Riken Keiki, AC-3). The *J-V* curves were obatined with scan rate 0.05 V/s under 1 sun with an AM 1.5G spectral filter (100 $mWcm^{-2}$)

coupled with maximum power point tracking (MPPT) system (SYSTEMHOUSE SUNRISE Corp). The *J-V* scans were carried out with scan rate 0.05 V/s in forward (*V* to V_{OC}) and reverse (V_{OC} to *V*) directions. The light intensity dependent J-V characteristics were obtained by *J-V* scan under 1 sun illumination with different filters. The stability of the encapsulated devices were monitored under standard illumination (AM1.5G, no UV-light filtering) following the maximum power point tracking (MPPT) condition. This system was equipped with a temperature-controlled oven coupled with solar simulator system (BIR-50; Bunko-keiki, Japan). The spectral responses were measured on SM-250 IPCE system (Bunko-keiki, Japan). Capacitance spectra (20 Hz to 2 MHz, Vac~0.03 V, 253 K to 343 K, under dark) were collected using an LCR meter (E4980A, Agilent). The temperature dependent characteristics was carried out by using the controlled chamber (SU-221) (±0.1 K).

ASSOCIATED CONTENT

Supporting Information

The Supporting Information is available free of charge on the ACS Publications website. Experimental Method, XRD patterns; Tabulated device parameters, absorption, transmission and photoelectron spectra of PCBM and CMC thin films, statistics of device parameters, J-V hysteresis plots, Reflectance spectra, Eg estimation form EQE, J-V characteristics with temperature and intensity, C-f-T spectra, Simulations data.

AUTHOR INFORMATION

Corresponding author.
*Email:KHADKA.B.Dhruba@nims.go.jp (D.B.K.)
*E-mail:SHIRAI.Yasuhiro@nims.go.jp (Y.S.)

ORCID
Dhruba B. Khadka: 0000-0001-9134-3890
Yasuhiro Shirai: 0000-0003-2164-5468

Masatoshi Yanagida: 0000-0002-8065-7875
Takeshi Noda: 0000-0002-6705-8552
Kenjiro Miyano: 0000-0002-5869-3087

Notes

The authors declare no competing financial interest.

ACKNOWLEDGEMENTS

This work was financially supported, in part, by MEXT Program for Development of Environmental Technology using Nanotechnology and the Japanese Society for the Promotion of Science (JSPS), KAKENHI (JP16K06285) and Advanced Low Carbon Technology Research and Development (ALCA) project of the Japan Science and Technology Agency (JST). The authors are grateful to Dr. Atsuko Nagataki for the technical support during XRD measurement.

REFERENCES

(1) Vos, A. De. Detailed Balance Limit of the Efficiency of Tandem Solar Cells. *J. Phys. D. Appl. Phys.* **1980**, *13* (5), 839–846.

(2) Todorov, T.; Gunawan, O.; Guha, S. A Road towards 25% Efficiency and beyond: Perovskite Tandem Solar Cells. *Mol. Syst. Des. Eng.* **2016**, *1* (4), 370–376.

(3) Lal, N. N.; White, T. P.; Catchpole, K. R. Optics and Light Trapping for Tandem Solar Cells on Silicon. *IEEE J. Photovoltaics* **2014**, *4* (6), 1380–1386.

(4) Shockley, W.; Queisser, H. J. Detailed Balance Limit of Efficiency of P-n Junction Solar Cells. *J. Appl. Phys.* **1961**, *32* (3), 510–519.

(5) Soga, T.; Kato, T.; Yang, M.; Umeno, M.; Jimbo, T. High Efficiency AlGaAs/Si Monolithic Tandem Solar Cell Grown by Metalorganic Chemical Vapor Deposition. *J.*

Appl. Phys. **1995**, *78* (6), 4196–4199.

(6) McMeekin, D. P.; Sadoughi, G.; Rehman, W.; Eperon, G. E.; Saliba, M.; Horantner, M. T.; Haghighirad, A.; Sakai, N.; Korte, L.; Rech, B.; Johnston, M. B.; Herz, L. M.; Snaith, H. J. A Mixed-Cation Lead Mixed-Halide Perovskite Absorber for Tandem Solar Cells. *Science* **2016**, *351* (6269), 151–155.

(7) Bush, K. A.; Palmstrom, A. F.; Yu, Z. J.; Boccard, M.; Cheacharoen, R.; Mailoa, J. P.; McMeekin, D. P.; Hoye, R. L. Z.; Bailie, C. D.; Leijtens, T.; Peters, I. M.; Minichetti, M. C.; Rolston, N.; Prasanna, R.; Sofia, S.; Harwood, D.; Ma, W.; Moghadam, F.; Snaith, H. J.; Buonassisi, T.; Holman, Z. C.; Bent, S. F.; McGehee, M. D. 23.6%-Efficient Monolithic Perovskite/Silicon Tandem Solar Cells With Improved Stability. *Nat. Energy* **2017**, *2* (4), 17009.

(8) Werner, J.; Weng, C. H.; Walter, A.; Fesquet, L.; Seif, J. P.; De Wolf, S.; Niesen, B.; Ballif, C. Efficient Monolithic Perovskite/Silicon Tandem Solar Cell with Cell Area >1 Cm2. *J. Phys. Chem. Lett.* **2016**, *7* (1), 161–166.

(9) Green, M. A.; Hishikawa, Y.; Dunlop, E. D.; Levi, D. H.; Hohl-Ebinger, J.; Ho-Baillie, A. W. Y. Solar Cell Efficiency Tables (Version 51). *Prog. Photovoltaics Res. Appl.* **2018**, *26* (1), 3–12.

(10) Noh, J. H.; Im, S. H.; Heo, J. H.; Mandal, T. N.; Seok, S. Il. Chemical Management for Colorful, Efficient, and Stable Inorganic-Organic Hybrid Nanostructured Solar Cells. *Nano Lett.* **2013**, *13* (4), 1764–1769.

(11) Yang, Z.; Rajagopal, A.; Jo, S. B.; Chueh, C. C.; Williams, S.; Huang, C. C.; Katahara, J. K.; Hillhouse, H. W.; Jen, A. K. Y. Stabilized Wide Bandgap Perovskite Solar Cells by Tin Substitution. *Nano Lett.* **2016**, *16* (12), 7739–7747.

(12) Hoke, E. T.; Slotcavage, D. J.; Dohner, E. R.; Bowring, A. R.; Karunadasa, H. I.; McGehee, M. D. Reversible Photo-Induced Trap Formation in Mixed-Halide Hybrid Perovskites for Photovoltaics. *Chem. Sci.* **2015**, *6* (1), 613–617.

(13) Kulkarni, S. A.; Baikie, T.; Boix, P. P.; Yantara, N.; Mathews, N.; Mhaisalkar, S. Band-Gap Tuning of Lead Halide Perovskites Using a Sequential Deposition Process. *J. Mater. Chem. A* **2014**, *2* (24), 9221–9225.

(14) Hu, M.; Bi, C.; Yuan, Y.; Bai, Y.; Huang, J. Stabilized Wide Bandgap MAPbBr x I 3– x Perovskite by Enhanced Grain Size and Improved Crystallinity. *Adv. Sci.* **2015**, *3*, 1500301.

(15) Lin, Y.; Chen, B.; Zhao, F.; Zheng, X.; Deng, Y.; Shao, Y.; Fang, Y.; Bai, Y.; Wang, C.; Huang, J. Matching Charge Extraction Contact for Wide-Bandgap Perovskite Solar Cells. *Adv. Mater.* **2017**, *29* (26), 1700607.

(16) Mailoa, J. P.; Bailie, C. D.; Johlin, E. C.; Hoke, E. T.; Akey, A. J.; Nguyen, W. H.; McGehee, M. D.; Buonassisi, T.; Strandberg, R.; Futscher, M. H.; Ehrler, B.; Soga, T.; Kato, T.; Yang, M.; Umeno, M.; Jimbo, T. Efficiency Limit of Perovskite/Si Tandem Solar Cells. *Appl. Phys. Lett.* **2015**, *106* (12), 4196–4199.

(17) Forgács, D.; Pérez-del-Rey, D.; Ávila, J.; Momblona, C.; Gil-Escrig, L.; Dänekamp, B.; Sessolo, M.; Bolink, H. J. Efficient Wide Band Gap Double Cation – Double Halide Perovskite Solar Cells. *J. Mater. Chem. A* **2017**, *5* (7), 3203–3207.

(18) Saliba, M.; Matsui, T.; Seo, J.-Y.; Domanski, K.; Correa-Baena, J.-P.; Nazeeruddin, M. K.; Zakeeruddin, S. M.; Tress, W.; Abate, A.; Hagfeldt, A.; Grätzel, M. Cesium-Containing Triple Cation Perovskite Solar Cells: Improved Stability, Reproducibility and High Efficiency. *Energy Environ. Sci.* **2016**, *9* (6), 1989–1997.

(19) Li, Y.; Sun, W.; Yan, W.; Ye, S.; Rao, H.; Peng, H.; Zhao, Z.; Bian, Z.; Liu, Z.; Zhou, H.; Huang, C. 50% Sn-Based Planar Perovskite Solar Cell with Power Conversion Efficiency up to 13.6%. *Adv. Energy Mater.* **2016**, *6* (24), 1601353.

(20) Bi, C.; Yuan, Y.; Fang, Y.; Huang, J. Low-Temperature Fabrication of Efficient Wide-Bandgap Organolead Trihalide Perovskite Solar Cells. *Adv. Energy Mater.* **2015**, *5*, 1401616.

(21) You, J.; Meng, L.; Song, T.-B.; Guo, T.-F.; Yang, Y. (Michael); Chang, W.-H.; Hong, Z.; Chen, H.; Zhou, H.; Chen, Q.; Liu, Y.; De Marco, N.; Yang, Y. Improved Air Stability of Perovskite Solar Cells via Solution-Processed Metal Oxide Transport Layers. *Nat. Nanotechnol.* **2016**, *11*, 75–82.

(22) Ren, Y.-K.; Ding, X.-H.; Wu, Y.-H.; Zhu, J.; Hayat, T.; Alsaedi, A.; Xu, Y.-F.; Li, Z.-Q.; Yang, S.-F.; Dai, S.-Y. Temperature-Assisted Rapid Nucleation: A Facile Method to Optimize the Film Morphology for Perovskite Solar Cells. *J. Mater. Chem. A* **2017**, *5* (38), 20327–20333.

(23) Bi, D.; Tress, W.; Dar, M. I.; Gao, P.; Luo, J.; Renevier, C.; Schenk, K.; Abate, A.; Giordano, F.; Correa Baena, J.-P.; Decoppet, J.-D.; Zakeeruddin, S. M.; Nazeeruddin, M. K.; Gra tzel, M.; Hagfeldt, A. Efficient Luminescent Solar Cells Based on Tailored Mixed-Cation Perovskites. *Sci. Adv.* **2016**, *2* (1), e1501170–e1501170.

(24) Yuchuan, S.; Yuan, Y.; Jinsong, H. Correlation of Energy Disorder and Open-Circuit Voltage in Hybrid Perovskite Solar Cells. *Nat. Energy* **2016**, *1* (3), 15001.

(25) Saliba, M.; Matsui, T.; Domanski, K.; Seo, J.-Y.; Ummadisingu, A.; Zakeeruddin, S. M.; Correa-Baena, J.-P.; Tress, W. R.; Abate, A.; Hagfeldt, A.; Gratzel, M. Incorporation of Rubidium Cations into Perovskite Solar Cells Improves Photovoltaic Performance. *Science* **2016**, *354* (6309), 206–209.

(26) Draguta, S.; Sharia, O.; Yoon, S. J.; Brennan, M. C.; Morozov, Y. V.; Manser, J. M.; Kamat, P. V.; Schneider, W. F.; Kuno, M. Rationalizing the Light-Induced Phase Separation of Mixed Halide Organic-Inorganic Perovskites. *Nat. Commun.* **2017**, *8*, 200.

(27) Zhang, B.; Guo, F.; Xue, J.; Yang, L.; Zhao, Y.; Ge, M.; Cai, Q.; Liu, B.; Xie, Z.; Chen, D.; Lu, H.; Zhang, R.; Zheng, Y. Photoluminescence Study of the Photoinduced Phase Separation in Mixed-Halide Hybrid Perovskite CH3NH3Pb(BrxI1−x)3 Crystals Synthesized via a Solvothermal Method. *Sci. Rep.* **2017**, *7* (1), 17695.

(28) Brivio, F.; Caetano, C.; Walsh, A. Thermodynamic Origin of Photoinstability in the CH3NH3Pb(I1-XBrx)3 Hybrid Halide Perovskite Alloy. *J. Phys. Chem. Lett.* **2016**, *7* (6), 1083–1087.

(29) Bischak, C. G.; Hetherington, C. L.; Wu, H.; Aloni, S.; Ogletree, D. F.; Limmer, D. T.; Ginsberg, N. S. Origin of Reversible Photoinduced Phase Separation in Hybrid Perovskites. *Nano Lett.* **2017**, *17* (2), 1028–1033.

(30) Slotcavage, D. J.; Karunadasa, H. I.; McGehee, M. D. Light-Induced Phase Segregation in Halide-Perovskite Absorbers. *ACS Energy Lett.* **2016**, *1* (6), 1199–1205.

(31) Khadka, D. B.; Shirai, Y.; Yanagida, M.; Masuda, T.; Miyano, K. Enhancement in Efficiency and Optoelectronic Quality of Perovskite Thin Films Annealed in MACl Vapor. *Sustain. Energy Fuels* **2017**, *1*, 755–766.

(32) Khadka, D. B.; Shirai, Y.; Yanagida, M.; Ryan, J. W.; Miyano, K. Exploring the Effects of Interfacial Carrier Transport Layers on Device Performance and Optoelectronic Properties of Planar Perovskite Solar Cells. *J. Mater. Chem. C* **2017**, *5*, 8819–8827.

(33) Tu, Y.; Wu, J.; Lan, Z.; He, X.; Dong, J.; Jia, J.; Guo, P.; Lin, J.; Huang, M.; Huang, Y. Modulated CH(3)NH(3)PbI(3−x)Br(x) Film for Efficient Perovskite Solar Cells Exceeding 18%. *Sci. Rep.* **2017**, *7*, 44603.

(34) Belisle, R. A.; Jain, P.; Prasanna, R.; Leijtens, T.; McGehee, M. D. Minimal Effect of the Hole-Transport Material Ionization Potential on the Open-Circuit Voltage of Perovskite Solar Cells. *ACS Energy Lett.* **2016**, *1* (3), 556–560.

(35) Wang, Q.; Chueh, C. C.; Eslamian, M.; Jen, A. K. Y. Modulation of PEDOT:PSS PH for Efficient Inverted Perovskite Solar Cells with Reduced Potential Loss and Enhanced Stability. *ACS Appl. Mater. Interfaces* **2016**, *8* (46), 32068–32076.

(36) Liu, T.; Jiang, F.; Qin, F.; Meng, W.; Jiang, Y.; Xiong, S.; Tong, J.; Li, Z.; Liu, Y.; Zhou, Y. Nonreduction Active Hole-Transporting Layers Enhancing Open-Circuit Voltage and Efficiency of Planar Perovskite Solar Cells. *ACS Appl. Mater. Interfaces* **2016**, *8*, 33899−33906.

(37) Jeon, N. J.; Noh, J. H.; Kim, Y. C.; Yang, W. S.; Ryu, S.; Seok, S. Il. Solvent Engineering for High-Performance Inorganic-Organic Hybrid Perovskite Solar Cells. *Nat. Mater.* **2014**, *13*, 897–903.

(38) Ren, Y.-K.; Shi, X.-Q.; Ding, X.-H.; Zhu, J.; Hayat, T.; Alsaedi, A.; Li, Z.-Q.; Xu, X.-X.; Yang, S.-F.; Dai, S.-Y. Facile Fabrication of Perovskite Layers with Large Grains through a Solvent Exchange Approach. *Inorg. Chem. Front.* **2018**, *5* (2), 348–353.

(39) Barker, A. J.; Sadhanala, A.; Deschler, F.; Gandini, M.; Senanayak, S. P.; Pearce, P. M.; Mosconi, E.; Pearson, A. J.; Wu, Y.; Srimath Kandada, A. R.; Leijtens, T.; De Angelis, F.; Dutton, S. E.; Petrozza, A.; Friend, R. H. Defect-Assisted Photoinduced Halide Segregation in Mixed-Halide Perovskite Thin Films. *ACS Energy Lett.* **2017**, *2* (6), 1416–1424.

(40) Junghwan, K.; I., S. M.; Hairen, T.; Yicheng, Z.; Younghoon, K.; Jongmin, C.; Woong, J. J.; James, F.; Rafael, Q.; Zhenyu, Y.; Na, Q. L.; Mingyang, W.; Oleksandr, V.; H., S. E. Amide-Catalyzed Phase-Selective Crystallization Reduces Defect Density in Wide-Bandgap Perovskites. *Adv. Mater.* **2018**, *30* (13), 1706275.

(41) Correa-Baena, J.-P.; Tress, W.; Domanski, K.; Anaraki, E. H.; Turren-Cruz, S.-H.; Roose, B.; Boix, P. P.; Grätzel, M.; Saliba, M.; Abate, A.; Hagfeldt, A. Identifying and Suppressing Interfacial Recombination to Achieve High Open-Circuit Voltage in Perovskite Solar Cells. *Energy Environ. Sci.* **2017**, *10* (5), 1207–1212.

(42) Shin, S. S.; Yang, W. S.; Noh, J. H.; Suk, J. H.; Jeon, N. J.; Park, J. H.; Kim, J. S.; Seong, W. M.; Seok, S. Il. High-Performance Flexible Perovskite Solar Cells Exploiting Zn2SnO4 Prepared in Solution below 100 °C. *Nat. Commun.* **2015**, *6*, 7410.

(43) Wojciechowski, K.; Saliba, M.; Leijtens, T.; Abate, A.; Snaith, H. J. Sub-150 [Degree]C Processed Meso-Superstructured Perovskite Solar Cells with Enhanced Efficiency. *Energy Environ. Sci.* **2014**, *7* (3), 1142–1147.

(44) Ke, W.; Fang, G.; Liu, Q.; Xiong, L.; Qin, P.; Tao, H.; Wang, J.; Lei, H.; Li, B.; Wan, J.; Yang, G.; Yan, Y. Lowerature Solution-Processed Tin Oxide as an Alternative Electron Transporting Layer for Efficient Perovskite Solar Cells. *J. Am. Chem. Soc.* **2015**, *137* (21), 6730–6733.

(45) Shao, Y.; Xiao, Z.; Bi, C.; Yuan, Y.; Huang, J. Origin and Elimination of Photocurrent Hysteresis by Fullerene Passivation in CH3NH3PbI3 Planar Heterojunction Solar Cells. *Nat. Commun.* **2014**, *5*, 5784.

(46) Zhu, Z.; Chueh, C. C.; Lin, F.; Jen, A. K.-Y. Enhanced Ambient Stability of Efficient Perovskite Solar Cells by Employing a Modified Fullerene Cathode Interlayer. *Adv. Sci.* **2016**, *3* (9), 1600027.

(47) Bai, Y.; Dong, Q.; Shao, Y.; Deng, Y.; Wang, Q.; Shen, L.; Wang, D.; Wei, W.; Huang, J. Enhancing Stability and Efficiency of Perovskite Solar Cells with Crosslinkable Silane-Functionalized and Doped Fullerene. *Nat. Commun.* **2016**, *7*, 12806.

(48) Li, Y.; Zhao, Y.; Chen, Q.; Yang, Y.; Liu, Y.; Hong, Z.; Liu, Z.; Hsieh, Y. T.; Meng, L.; Li, Y.; Yang, Y. Multifunctional Fullerene Derivative for Interface Engineering in Perovskite Solar Cells. *J. Am. Chem. Soc.* **2015**, *137* (49), 15540–15547.

(49) Xu, J.; Buin, A.; Ip, A. H.; Li, W.; Voznyy, O.; Comin, R.; Yuan, M.; Jeon, S.; Ning, Z.; McDowell, J. J.; Kanjanaboos, P.; Sun, J.-P.; Lan, X.; Quan, L. N.; Kim, D. H.; Hill, I. G.; Maksymovych, P.; Sargent, E. H. Perovskite–fullerene Hybrid Materials Suppress Hysteresis in Planar Diodes. *Nat. Commun.* **2015**, *6*, 7081.

(50) Tripathi, N.; Yanagida, M.; Shirai, Y.; Masuda, T.; Han, L.; Miyano, K. Hysteresis-Free and Highly Stable Perovskite Solar Cells Produced via a Chlorine-Mediated Interdiffusion Method. *J. Mater. Chem. A* **2015**, *3*, 12081–12088.

(51) Wienk, M. M.; Kroon, J. M.; Verhees, W. J. H.; Knol, J.; Hummelen, J. C.; van Hal, P. A.; Janssen, R. A. J. Efficient Methano [70] Fullerene/MDMO-PPV Bulk Heterojunction Photovoltaic Cells. *Angew. Chemie* **2003**, *42*, 3493–3497.

(52) Nakanishi, R.; Nogimura, A.; Eguchi, R.; Kanai, K. Electronic Structure of Fullerene Derivatives in Organic Photovoltaics. *Org. Electron.* **2014**, *15* (11), 2912–2921.

(53) Park, S. H.; Roy, A.; Beaupré, S.; Cho, S.; Coates, N.; Moon, J. S.; Moses, D.; Leclerc, M.; Lee, K.; Heeger, A. J. Bulk Heterojunction Solar Cells with Internal Quantum Efficiency Approaching 100%. *Nat. Photonics* **2009**, *3* (5), 297–302.

(54) Hu, M.; Bi, C.; Yuan, Y.; Xiao, Z.; Dong, Q.; Shao, Y.; Huang, J. Distinct Exciton

Dissociation Behavior of Organolead Trihalide Perovskite and Excitonic Semiconductors Studied in the Same System. *Small* **2015**, *11* (18), 2164–2169.

(55) Chikamatsu, M.; Nagamatsu, S.; Yoshida, Y.; Saito, K.; Yase, K.; Kikuchi, K. Solution-Processed n -Type Organic Thin-Film Transistors with High Field-Effect Mobility. *Appl. Phys. Lett.* **2005**, *87*, 203504.

(56) Horii, Y.; Ikawa, M.; Chikamatsu, M.; Azumi, R.; Kitagawa, M.; Konishi, H.; Yase, K. Soluble Fullerene-Based n-Channel Organic Thin-Film Transistors Printed by Using a Polydimethylsiloxane Stamp. *ACS Appl. Mater. Interfaces* **2011**, *3* (3), 836–841.

(57) Mas-Torrent, M.; Rovira, C. Novel Small Molecules for Organic Field-Effect Transistors: Towards Processability and High Performance. *Chem. Soc. Rev.* **2008**, *37* (4), 827.

(58) Chikamatsu, M.; Itakura, A.; Yoshida, Y.; Azumi, R.; Yase, K. High-Performance n-Type Organic Thin-Film Transistors Based on Solution-Processable Perfluoroalkyl-Substituted C60 Derivatives. *Chem. Mater.* **2008**, *20* (24), 7365–7367.

(59) Horii, Y.; Sakaguchi, K.; Chikamatsu, M.; Azumi, R.; Yase, K.; Kitagawa, M.; Konishi, H. High-Performance Solution-Processed n-Channel Organic Thin-Film Transistors Based on a Long Chain Alkyl-Substituted C60 Derivative. *Appl. Phys. Express* **2010**, *3*, 101601.

(60) Nayak, P. K.; Garcia-Belmonte, G.; Kahn, A.; Bisquert, J.; Cahen, D. Photovoltaic Efficiency Limits and Material Disorder. *Energy Environ. Sci.* **2012**, *5* (3), 6022–6039.

(61) Würfel, U.; Neher, D.; Spies, A.; Albrecht, S. Impact of Charge Transport on Current–voltage Characteristics and Power-Conversion Efficiency of Organic Solar Cells. *Nat.*

Commun. **2015**, *6*, 6951.

(62) Christians, J. A.; Schulz, P.; Tinkham, J. S.; Schloemer, T. H.; Harvey, S. P.; Tremolet de Villers, B. J.; Sellinger, A.; Berry, J. J.; Luther, J. M. Tailored Interfaces of Unencapsulated Perovskite Solar Cells for >1,000 Hour Operational Stability. *Nat. Energy* **2018**, *3* (1), 68–74.

(63) Grancini, G.; Zimmermann, I.; Mosconi, E.; Martineau, D.; Narbey, S. One-Year Stable Perovskite Solar Cells by 2D / 3D Interface Engineering. *Nat Commun* **2017**, *8*, 15684.

(64) Cheng, L.; Yi, Y.; Yong, D.; Jia, X.; Xiaolong, L.; Bing, Z.; Jianxi, Y.; Tasawar, H.; Ahmed, A.; Dai, S.-Y. High-Efficiency and UV-Stable Planar Perovskite Solar Cells Using a Low-Temperature, Solution-Processed Electron-Transport Layer. *ChemSusChem* **2018**, *11* (7), 1232–1237.

(65) Deng, Y.; Dong, Q.; Bi, C.; Yuan, Y.; Huang, J. Air-Stable , Efficient Mixed-Cation Perovskite Solar Cells with Cu Electrode by Scalable Fabrication of Active Layer. *Adv. Energy Mater.* **2016**, 1600372.

(66) Cowan, S. R.; Roy, A.; Heeger, A. J. Recombination in Polymer-Fullerene Bulk Heterojunction Solar Cells. *Phys. Rev. B* **2010**, *82*, 245207.

(67) Poglitsch, A.; Weber, D. Dynamic Disorder in Methylammoniumtrihalogenoplumbates (II) Observed by Millimeter-Wave Spectroscopy Dynamic Disorder in Methylammoniumtrihalogenoplumbates (II) Observed by Millimeter-Wave Spectroscopy. *J. Chem. Phys.* **1987**, *87*, 6373–6378.

(68) Hegedus, S. S.; Shafarman, W. N. Thin-Film Solar Cells: Device Measurements and Analysis. *Prog. Photovoltaics Res. Appl.* **2004**, *12*, 155–176.

(69) Khadka, D. B.; Shirai, Y.; Yanagida, M.; Miyano, K. Degradation of Encapsulated Perovskite Solar Cells Driven by Deep Trap States and Interfacial Deterioration. *J. Mater. Chem. C* **2018**, *6*, 162–170.

(70) Hu, Z.; Miao, J.; Li, T.; Liu, M.; Murtaza, I.; Meng, H. Reduced Interface Losses in Inverted Perovskite Solar Cells by Using a Simple Dual-Functional Phenanthroline Derivative. *Nano Energy* **2018**, *43*, 72–80.

(71) Walter, T.; Herberholz, R.; Müller, C.; Schock, H. W. Determination of Defect Distributions from Admittance Measurements and Application to Cu(In,Ga)Se2 Based Heterojunctions. *J. Appl. Phys.* **1996**, *80* (8), 4411–4420.

(72) Khadka, D. B.; Kim, S.; Kim, J. Effects of Ge Alloying on Device Characteristics of Kesterite-Based CZTSSe Thin Film Solar Cells. *J. Phys. Chem. C* **2016**, *120*, 4251–4258.

(73) Jahandar, M.; Heo, J. H.; Song, C. E.; Kong, K.-J.; Shin, W. S.; Lee, J.-C.; Im, S. H.; Moon, S.-J. Highly Efficient Metal Halide Substituted CH3NH3I(PbI2)1-X(CuBr2)X Planar Perovskite Solar Cells. *Nano Energy* **2016**, *27*, 330–339.

(74) Duan, H.; Zhou, H.; Chen, Q.; Sun, P.; Luo, S.; Song, T.; Bob, B.; Yang, Y. The Identification and Characterization of Defect States in Hybrid Organic – Inorganic Perovskite. *Phys. Chem. Chem. Phys.* **2015**, *17*, 112–116.

(75) Burgelman, M.; Nollet, P.; Degrave, S. Modelling Polycrystalline Semiconductor Solar Cells. *Thin Solid Films* **2000**, *361*, 527–532.

Table of Contents Graphics